Desalination and Water Treatment
www.deswater.com
doi: 10.5004/dwt.2020.26194

203 (2020) 137–149
November

A new porous Ag_3PO_4/(Cs, Rb)$_x$$WO_3$/g-$C_3N_4$/CoAl-LDH composite towards efficient photocatalytic degradation of phenol and its derivatives

Caifeng Li[a], Yinke Wang, Guoqing Zhao, Tao Yan, Taiheng Zhang, Lukai Liu, Feipeng Jiao*, Jian Huang*

School of Chemistry and Chemical Engineering, Central South University, Changsha 410083, China, Tel. +86 731 88830833; Fax: +86 731 88830833; emails: jiaofp@csu.edu.cn (F. Jiao), jhuang821@126.com (J. Huang)

Received 16 October 2019; Accepted 3 June 2020

ABSTRACT

In this work, a new porous Ag_3PO_4/(Cs, Rb)$_x$$WO_3$/g-$C_3N_4$/CoAl-LDH (CoAl-LDH – CoAl-layered double hydroxide) composite was synthesized through a facile method and utilized as a photocatalyst towards efficient photocatalytic degradation of phenol and its derivatives, 2-chlorophenol (2-CP) and 2-nitrophenol (2-NP). A series of characterization and experiments results showed the resultant composite had excellent structure and outstanding performance, 2-NP was degraded most completely, followed by 2-CP and finally phenol. Furthermore, the composite still remained favorable stability after five cycles and the possible photocatalytic degradation mechanism was proposed. This paper provided a new idea for the preparation of novel photocatalysts.

Keywords: Porous composite; Layered double hydroxides; Photocatalytic degradation; Phenol; 2-chlorophenol; 2-nitrophenol

1. Introduction

Currently, largish interest has been invested to dispose of phenol and its derivatives, because of their high virulence and carcinogenicity in many industrial activities, such as cosmetics, disinfectants, herbicides, pesticides and artificial resins [1–3]. In 1976 eleven phenolic compounds were detailed in the United States Environmental Protection Agency prior pollutant list [4], among which the derivatives of phenol like chlorophenols and nitrophenols are deemed as a potential danger for their toxic nature. The massive discharge of these pollutants into the environment will lead to severe contamination to the aquatic system [5]. Furthermore, anthropogenic activities and unconscionable sewage disposal result in the more consecutive discharge of phenol and its derivatives to aquatic environments. Therefore, an easy and effective methodology that can simultaneously remove both chlorophenols and nitrophenols is important for water remediation. Currently, the photocatalytic degradation technology has been considered the most feasible route for decomposing phenol and its derivatives via utilizing versatile photocatalysts [6,7].

Among the reported hierarchical semiconductor photocatalyst, CoAl-layered double hydroxide (CoAl-LDH) is regarded as a promising photocatalyst, because it has a convenient cost, avirulence, appropriate oxidation-reduction electric potential and outstanding photochemical absorption performance [8–10]. However, the practical application of CoAl-LDH is hampered by its inherent defects, such as weak conductivity, low energy conversion efficiency and so forth [11]. In order to handle the above issues, multiple methodologies have been exploited to design CoAl-LDH-based structurally modulated heterostructures to enhance photocatalytic activities [12,13]. Recent literature provided a

* Corresponding authors.

novel and facile strategy to boost the photocatalytic properties of LDH by coupling it with several hierarchical semiconductor materials, which drastically render high-efficiency physical contact and a strong electronic coupling [14,15], and g-C_3N_4 is a preferential candidate because of its similar laminar structure to LDH. Besides, the unique delocalized conjugated π structures of g-C_3N_4 can notably improve the charge separation efficiency, improving the stability and photocatalytic performance of LDH [16,17]. Regrettably, the heterostructure formed by LDH and g-C_3N_4 is still a problem because there is often the toilless formation of irreversible agglomerates, and the inferior stability of powdered photocatalysts seriously limit their application [18].

To dispose these questions and further obtain exceptionally effective charge transport, fabricating a heterojunction through collaborating with Ag-based photocatalysts is substantiated to be one feasible approach. Ag_3PO_4 is the optimal candidate for it admittedly possesses the highest quantum efficiency and presents distinctive photocatalytic activities toward hazardous organic pollutant degradation [19–21]. Cs_xWO_3 (a tungsten bronze type nanocrystal) is another preferential candidate for photocatalysis by right of its excellent optical absorption performance in a wide range including the UV, Vis and NIR region and distinctive conductivity. Beyond these, the existent mixed chemical valence of W^{6+} and W^{5+}, oxygen vacancies and free-electron also accelerate the immigration of photogenerated charges by forming localized states underneath the conduction band [22–25]. Recently, several researches manifested that the co-doped structure by introducing double cations into the M point of tungsten bronze can increase the free electrons in the conduction band, improve the lattice distortion degree and reduce the release of doped ions, thus significantly improving the selective light transmittance and structural stability of tungsten bronze [26–29]. Introducing Cs and Rb simultaneously to form co-doped tungsten bronze has not been studied. Except for the above measures, the creating of porous structures is a convenient and effective approach based on energy absorption to improve photocatalytic performance through speeding up the mass transfer and enhancing exciton dissociation efficiency, which will also significantly slow the toilless formation of irreversible agglomerates, increase the photoactive sites and the inaccessibility of internal surfaces of the synthetic samples for facile charge transfer, hence seriously improving the spring-board for fabricating and exploring new-fashioned and multifunctional photocatalyst, which shows an enticing prospect in photochemical reactions and energy conversion.

In this work, a novel porous Ag_3PO_4/(Cs, Rb)$_x$$WO_3$/g-$C_3N_4$/CoAl-LDH composite was successfully synthesized. Ag_3PO_4, (Cs, Rb)$_x$$WO_3$ and g-C_3N_4 were introduced to improve the photocatalytic activity of CoAl-LDH. Phenol and its derivatives, 2-chlorophenol (2-CP) and 2-nitrophenol (2-NP) were regarded as model pollutants to evaluate the photocatalytic performance of prepared photocatalysts, and Ag_3PO_4/(Cs, Rb)$_x$$WO_3$/g-$C_3N_4$/CoAl-LDH exhibited favorable degradation efficiency. This work provides a novel strategy to enhance the catalytic activity of photocatalysts, which also provides a useful concept for the design of economical and efficient catalysts.

2. Experimental section

2.1. Materials

Cobalt nitrate hexahydrate (>98.5%, Sinopharm Chemical Reagent Co., Ltd., China), aluminum nitrate nonahydrate (>99%, Guangdong Jinhuada Chemical Reagent Co., Ltd., China), silver nitrate (>99.8%, Sinopharm Chemical Reagent Co., Ltd., China), rubidium chloride (AR degrade, Tianjin Guangfu Fine Chemical Research Institute, China), cesium hydroxide monohydrate (>99%, Adamas Reagent Co., Ltd., China), tungsten hexachloride (AR degrade, Alfa Aesar, China), diammonium hydrogen phosphate (>99%, Sinopharm Chemical Reagent Co., Ltd., China), dicyandiamide (>99%, Sinopharm Chemical Reagent Co., Ltd., China), phenol (Alfa Aesar, China), 2-chlorophenol (Saen Technology Co., Ltd., China), 2-nitrophenol (Alfa Aesar, China).

2.2. Synthesis of Ag_3PO_4/(Cs, Rb)$_x$$WO_3$/g-$C_3N_4$/CoAl-LDH (AWCL)

The CoAl-LDH, (Cs, Rb)$_x$$WO_3$/CoAl-LDH and Ag_3PO_4/(Cs, Rb)$_x$$WO_3$/CoAl-LDH were synthesized in advance (supporting information). For AWCL composite (scheme 1), 0.2 g the resultant Ag_3PO_4/(Cs, Rb)$_x$$WO_3$/CoAl-LDH particles were ultrasonically dispersed in 50 mL saturated dicyandiamide solution. Pieces of soft cubic PU sponges (0.5 cm × 0.5 cm × 0.5 cm) were adequately impregnated into the above suspension with moderately stirring. After approximately 2 h adsorption, the polyurethane sponges (PU sponges) were placed at 80°C to evaporated the liquid completely. Repeatedly operating these process several times to make the PU sponges enrich the suspension adequately. The ultima Ag_3PO_4/(Cs, Rb)$_x$$WO_3$/g-$C_3N_4$/CoAl-LDH was obtained through calcining the obtained PU sponges in a tube furnace in 550°C for 1 h (5°C min^{-1}). The hierarchically porous g-C_3N_4 was synthesized only using PU sponges and saturated dicyandiamide solution, and the bulk g-C_3N_4 was also synthesized through direct heating dicyandiamide at 550°C for 4 h as a contrast.

2.3. Characterization

The crystal structures of the samples were measured through X-ray powder diffraction (XRD, Bruker D8). The morphologies were examined via scanning electron microscopy (SEM, TESCAN MIRA3 LMU) equipped with the energy-dispersive X-ray spectroscopy analysis system. The chemical constitutions and valence band spectrum were investigated using X-ray photoelectron spectroscopy (XPS, ESCALAB 250Xi). The Fourier-transform infrared spectra were recorded on an AVATAR 360 spectrometer. The steady-state UV-vis absorption and UV-vis diffused reflectance spectra (UV-vis DRS) were obtained by a UV-vis spectrophotometer (Shimadzu 2401 model). The pore size distributions and Brunauer–Emmett–Teller (BET) were evaluated through nitrogen adsorption isotherms.

2.4. Photocatalytic activity tests

For typical photocatalytic runs, the photocatalytic activities of the obtained samples were investigated by photocatalytic removing varied contaminants under visible

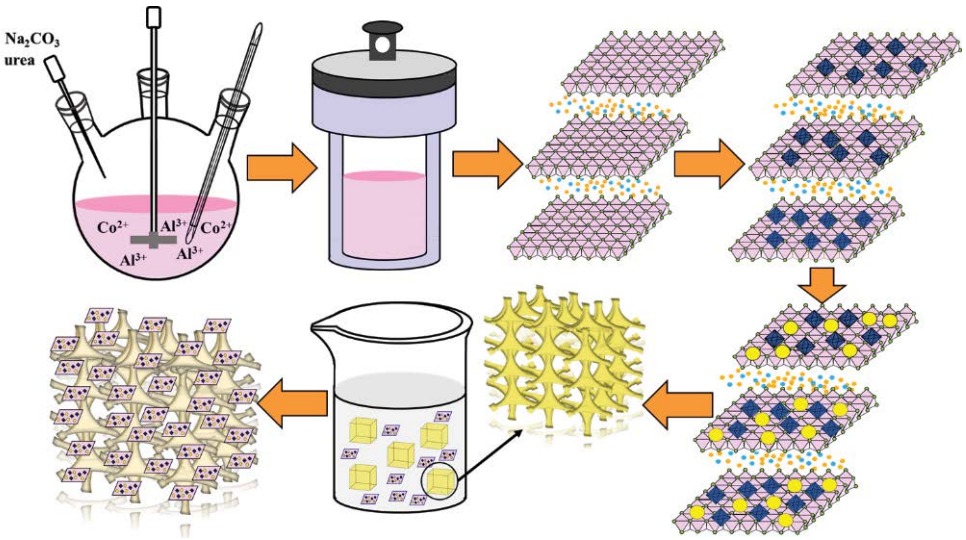

Scheme 1. Schematic illustration of the synthesis process of AWCL composite.

light. In this experiment, phenol, 2-CP, 2-NP and a mixture of the above three pollutants were used as model pollutants, and a 500 W Xe lamp equipped with a full spectrum cut-off glass filter was employed as the simulated solar light source. Before light irradiation, the suspensions were moderately stirred in dark for 30 min to reach adsorption–desorption equilibrium ulteriorly. Thereafter turning on the 500 W Xe lamp, about 3 mL mixed solution was sampled and detected using a UV-vis spectrophotometer at a fixed interval. Simultaneously, a blank experiment under dark condition or no catalyst was carried out to explore the effects of absorption between photocatalysis and pollutant molecules causing by strong electrostatic attraction in accordance with the Langmuir adsorption.

3. Results and discussion

3.1. Characterization of the as-prepared materials

The phase identification of all the as-synthesized materials was analyzed by XRD measurement and presented in Fig. 1. The sharp characteristic peaks of g-C_3N_4 and Ag_3PO_4 rendered other peaks not prominent. The XRD patterns of (Cs, Rb)$_x$WO$_3$ exhibited the characteristic peaks of both Cs_xWO_3 and Rb_xWO_3 without any other impurities, indicating the facile hydrothermal process was feasible to prepare the (Cs, Rb)$_x$WO$_3$ without significant structural and composition changes [30,31]. The CoAl-LDH XRD patterns presented various diffraction peaks at 2θ values of 11.3°, 23.4°, 34.7°, 39.2°, 46.6° and 60.1°, corresponding to (003), (006), (012), (015), (018) and (110) lattice planes, which indicated the CoAl-LDH belonged to the space group r3·m with a three-layer 3R polytypic rhombohedral symmetry and CO_3^{2-} was the intercalating anion [32,33]. After calculating according to the Bragg law, $2d\sin(\theta) = n\lambda$ [34], the interlamellar distance (d) in stacked CoAl-LDH was 0.76 nm, and the value of lattice parameter (a) was estimated to be about 0.32 nm. The g-C_3N_4 and g-C_3N_3 sponges exhibited similar XRD patterns with two typical

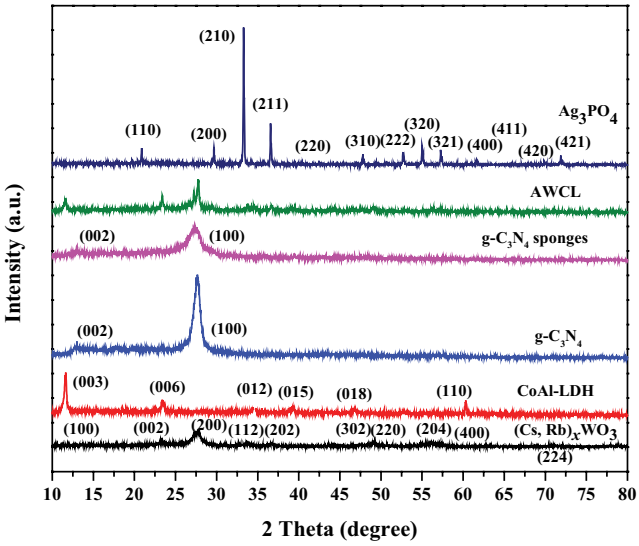

Fig. 1. XRD patterns of Ag_3PO_4, (Cs, Rb)$_x$WO$_3$, CoAl-LDH, g-C_3N_4, g-C_3N_4 sponges and AWCL composite.

diffraction peaks at 13° and 27°corresponding to (002) and (100) lattice planes respectively [35], which turned out the retention of the π-conjugated system [36,37]. Nevertheless, the g-C_3N_4 sponges had relatively broadened peaks, which was ascribed to the crystallographic changes induced by process-temperature in original g-C_3N_4 [38–40]. For Ag_3PO_4, the presented diffraction peaks accorded with a body-centered cubic phase (JCPDS NO.06–0505). Furthermore, the sharp and high-intensity diffraction peaks suggested the Ag_3PO_4 possessed high crystallinity. The AWCL composite presented a coexistence of Ag_3PO_4, (Cs, Rb)$_x$WO$_3$ and g-C_3N_4 sponges phases with no other impurities. The values of "a" and "c" on behalf of the unit cell directions of CoAl-LDH in AWCL were estimated to be 0.30 and 46 nm. The changes in "c" exposed Ag_3PO_4 and (Cs, Rb)

$_xWO_3$ successfully grew and distributed over the stacked exfoliated CoAl-LDH sheets with positively charged lamellar self-assembly structure and negatively charged g-C_3N_4 sponges.

The morphologies of the as-synthesized samples were investigated through SEM and the characterization results are shown in Fig. 2. The pristine CoAl-LDH displayed a prominent layer-by-layer structure, which was the typical characteristic of LDHs. The original g-C_3N_4 exhibited bulk morphologies without any obvious pores. Inversely the g-C_3N_4 disposed by PU sponges possessed distinct pores structure because the soft PU template would decompose and vaporize in the process of heating, the generated gases contributed to the formation of the pores. Simultaneously the shrinking of void stemming from the PU skeleton fibers' burning also promoted the formation of pore structures. The introduction of pores facilitated the penetration and absorption of visible light, accelerated the quality conversion in the pores of g-C_3N_4, therefore enhanced the photocatalytic activities. The new AWCL composite was synthesized by introducing the above advantages. In Fig. 2d, the AWCL composite displayed excellent morphologies with favorable dispersibility, the Ag_3PO_4 and (Cs, Rb)$_xWO_3$ could be dispersed over the surface of CoAl-LDH irregularly and the introducing of g-C_3N_4 sponges further increased the dispersion as well as absorption of visible light. Besides, Fig. S1 also proved the formation of the AWCL composite.

The nitrogen adsorption–desorption technique was employed to calculate the specific surface area and pore size distribution. As shown in Fig. 3a, the g-C_3N_4, g-C_3N_4 sponges and AWCL composite all accorded with type IV isotherm with H3 hysteresis loops, and the pore-size distribution curve displayed there were abundant mesopores intermingling with few micropores. Apparently, the g-C_3N_4 sponges possessed larger pore size in contrast to the pristine g-C_3N_4, which meant affluent large channels have been introduced into the surface of g-C_3N_4, therefore accelerated visible light infiltration and absorption. Beyond the mesoporous channels similar to g-C_3N_4 sponges, the AWCL composite had a lager BET surface area (65.2 $m^2 g^{-1}$) and a larger pore volume (0.724 0.57 $cm^3 g^{-1}$) than g-C_3N_4 and g-C_3N_4 sponges, which conformed with the SEM results (Table 1).

Regarding the enhancement mechanism of visible light absorption, the UV-visible diffuse reflection spectrum (UV-vis DRS) results further attested the AWCL composite achieved outstanding photoabsorption behaviors than other photocatalysts. As shown in Fig. 4, the (Cs, Rb)$_xWO_3$ had the best visible light absorption ability by virtue of its unique performance, which also assisted the AWCL composite to expend light regions. The g-C_3N_4 sponges obtained a wider absorption region of about 500 nm than g-C_3N_4, confirming the significance of pore architecture for light absorption. Besides, the micron pores and nanometer pores improved the photocatalytic performance in different aspects. The micron pores basically accelerated visible light into the nanometer pores followed into the photocatalyst, simultaneously the nano-pores mainly facilitated the light absorption on pore walls to expand the optical absorption regions [29]. Small bandgap energy (2.43 eV) render Ag_3PO_4 possesses excellent photocatalytic performance [17], thus the incorporation of Ag_3PO_4 notably

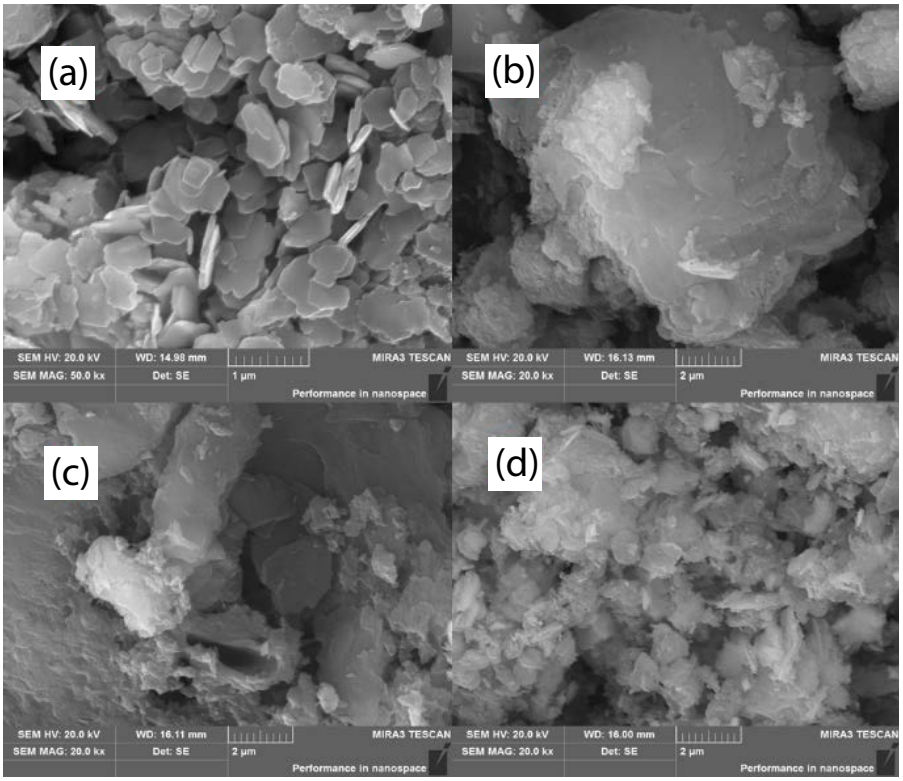

Fig. 2. SEM images of (a) CoAl-LDH, (b) g-C_3N_4, (c) g-C_3N_4 sponges and (d) AWCL composite.

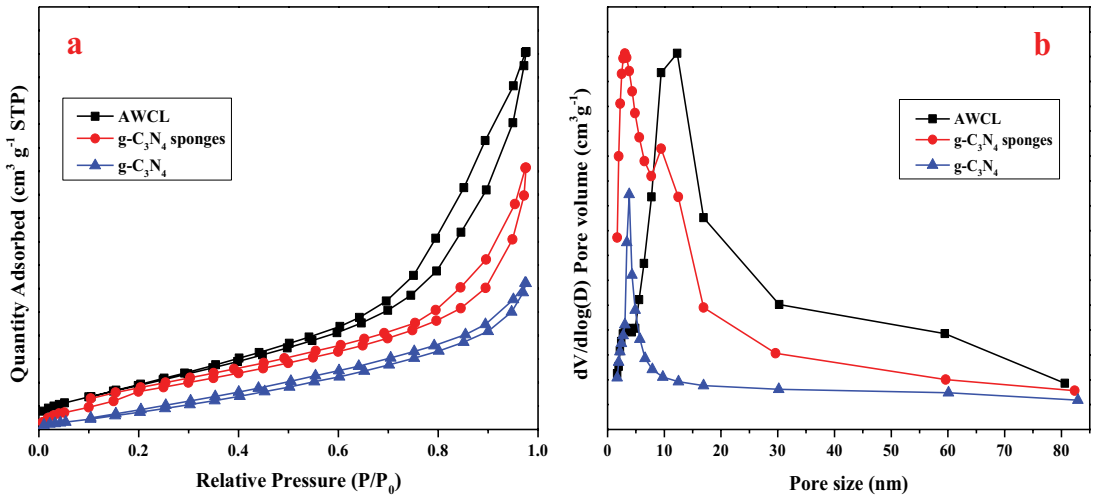

Fig. 3. (a) N_2 adsorption–desorption isotherms and (b) pore size distribution of g-C_3N_4, g-C_3N_4 sponges and AWCL composite.

Table 1
Texture properties of g-C_3N_4, g-C_3N_4 sponges and AWCL composite

Materials	BET area (m^2/g)	Centred pore size distribution (nm)	Pore volume (cm^{-3} g^{-1})
g-C_3N_4	10	5	0.247
g-C_3N_4 sponges	60.4	10	0.676
AWCL composite	65.2	15	0.724

influenced the optical properties of AWCL composite. Furthermore, Fig. 4b shows the bandgap of the AWCL composite was smaller than g-C_3N_4 and g-C_3N_4 sponges, more firmly certifying the AWCL composite owned favorable photoabsorption activity.

The XPS technique was regarded as a rigorous tool to detect the prepared samples' elementary composition and electronic environment. The XPS survey scan showed there were only Ag, Cs, Rb, Co, Al, P, O, W, C and N, elements existing in AWCL composite without other elements, conforming the AWCL composite was formed resoundingly (Supporting information Fig. S2). For Co 2p spectra, the two peaks centered at 783.3 and 796.7 eV were attributed to Co $2p_{3/2}$ and Co $2p_{1/2}$. Correspondingly, two symmetrical peaks at 61.3 and 73.8 eV corresponded to the Al 2p spectrum [41]. The C 1s peaks revealed three evident peaks at 284.2, 286.2 and 288 eV for C–C containing defect in graphitic carbon, C–NH_x and N=C–N respectively, and N 1s spectra presented three prominent peaks, which could be ascribed into C–N=C (397.5 eV), N–$(C)_3$ (398.2 eV) and –NH_2 (401 eV) [29,42]. As can be seen from Fig. 5c, the Ag 3d spectrum was divided into Ag^0 along with Ag^+ peaks. The former contained two main peaks at 368.2 and 374.2 eV, and the latter also possessed two peaks located at 367.8 and 373.8 eV [43,44]. For O 1s spectra, the peak at 530.6 eV was related to the lattice oxygen-O_2 in Ag_3PO_4, and another peak at 532.5 eV was connected with the absorbed water-O_4

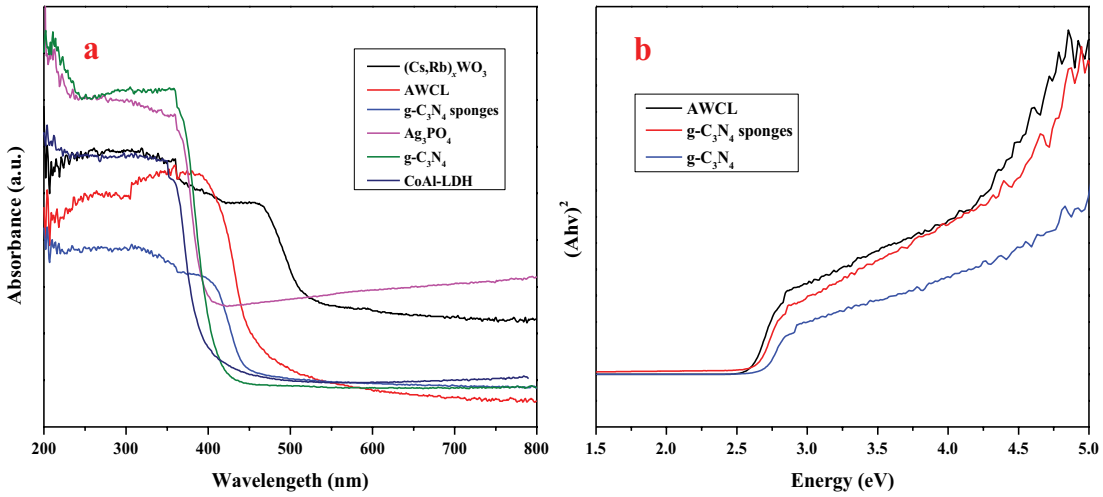

Fig. 4. (a) UV-Vis diffuse reflectance spectra and (b) energy band gaps of g-C_3N_4, g-C_3N_4 sponges and AWCL composite.

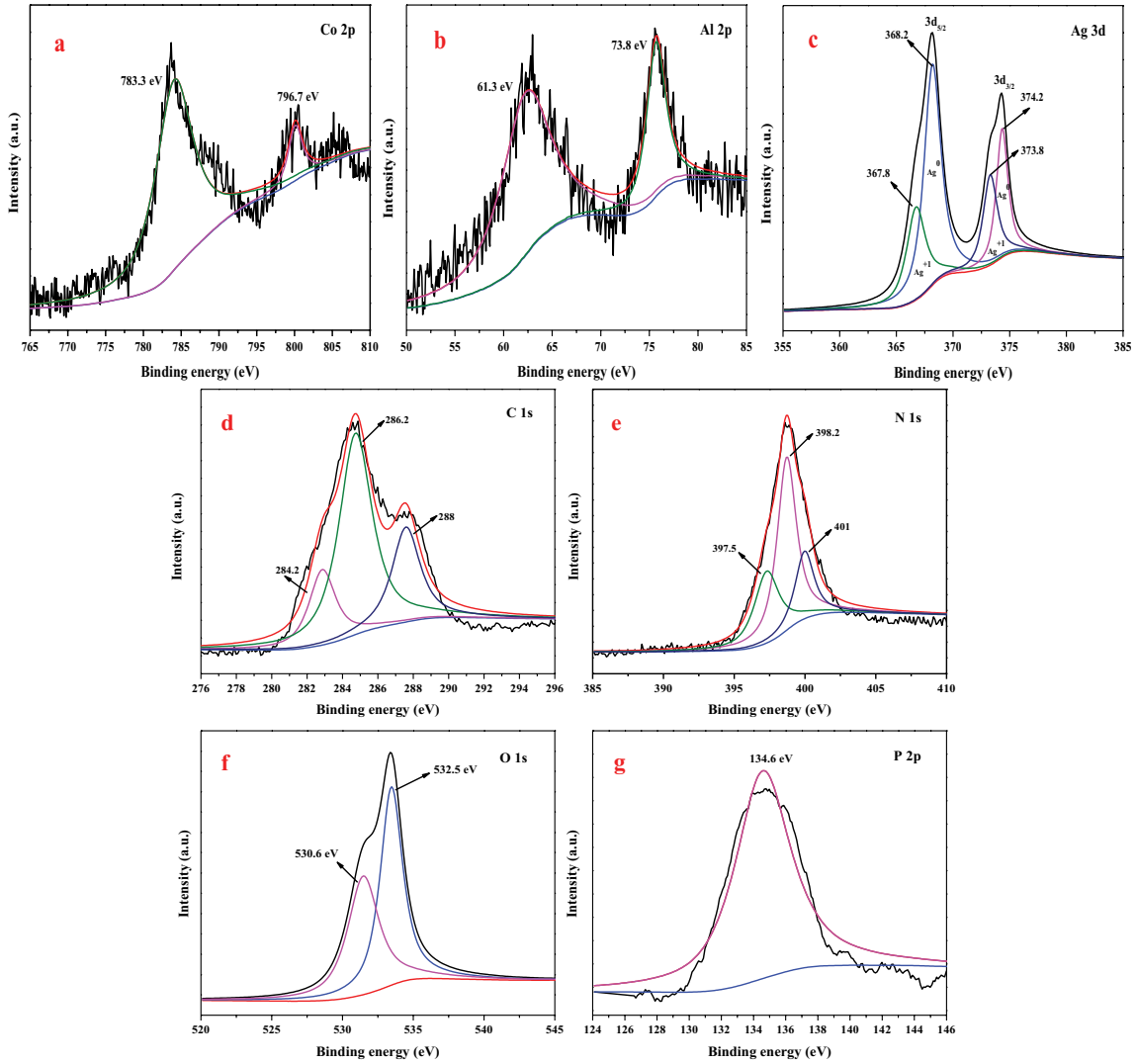

Fig. 5. XPS spectra of AWCL composite for (a) Co 2p, (b) Al 2p, (c) Ag 3d, (d) C 1s, (e) N 1s, (f) O 1s and (g) P 2p.

presented on the surface of AWCL composite. The P 2p only had one symmetrical peak centered at 134.6 eV, which was put down to the P^{+5} came from PO_4^{3-}.

3.2. Photocatalytic degradation of phenol and its derivatives

3.2.1. Photocatalytic degradation of phenol

The photocatalytic degradation capability of phenol with AWCL composite was evaluated and compared with CoAl-LDH, $(Cs, Rb)_xWO_3$, g-C_3N_4, g-C_3N_4 sponges and Ag_3PO_4. In Fig. 6a, only 17.6%, 12.5%, 11.0%, 14.5%, 17% and 13.3% removing efficiency were obtained in dark, manifesting the adsorption of catalysts played a negligible role in oxidizing phenol. After exposure with a light source, an evident decrease was achieved for pristine Ag_3PO_4 (86.4%), $(Cs, Rb)_xWO_3$ (43.8%), g-C_3N_4 (58.8%), g-C_3N_4 sponges (71.3%) and CoAl-LDH (53.7%), and the AWCL composite presented the notably outstanding photocatalytic effect (94.6%), convincingly elucidating the mutual effect between Ag_3PO_4, $(Cs, Rb)_xWO_3$, g-C_3N_4, g-C_3N_4 sponges, and CoAl-LDH occupied a significant place in photocatalytic degradation of phenol.

The photocatalytic degradation efficiencies of phenol in diverse pHs were also studied because the solution pH played a significant role in the existence of active substances. The solution pH was changed from 3 to 12, and the experiment results are shown in Fig. 6c. Obviously, the sequence of degradation efficiency was pH 7 > pH 3 > pH 5 > pH 9 > pH 12, the AWCL composite obtained the most prominent degradation efficiency at pH 7 and presented better removing effect in acidic solution than the basic solution. A strong base solution, the oxygen functional groups generated by AWCL composite were more liable to dissolve to make the structure of catalyst more unstable, thus tending to lose the photocatalytic activity and hamper the degradation efficiency.

To deeply research the reaction kinetic of degradation of phenol, the kinetics study of different catalysts was carried out and analyzed using a UV-visible spectrophotometer. The experimental results followed pseudo-first-order kinetic model, which can be expressed as below:

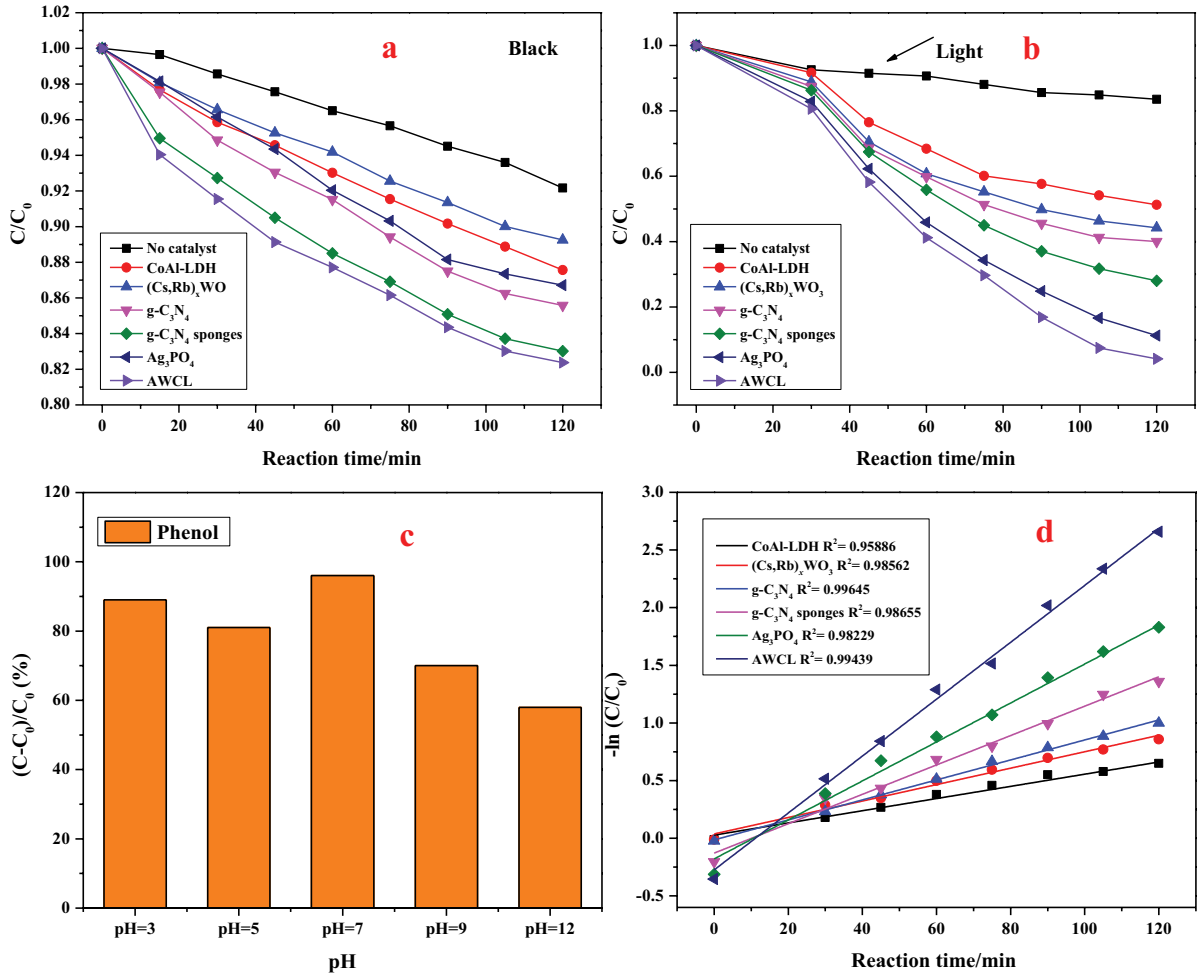

Fig. 6. Adsorption of phenol with different catalysts in the dark (a), photocatalytic degradation of phenol with different catalysts in visible light (b), the influence of pH on degradation of phenol with AWCL composite (c) and pseudo-first-order degradation kinetics for phenol with different catalysts (d).

$$\frac{C}{C_0} = e^{-kt} \quad (1)$$

where k is the reaction rate constant in min^{-1}, C_0 stands the original concentration and C represents the ultima concentration at instantaneous time t. The change curve of $\ln(C/C_0)$ over time can be synthesized into a straight line by linearly fitting the regression curve, and the corresponding rate constants k, coefficient of determinations (R^2), and standard errors are tabulated in Table 2. After being calculated, the AWCL composite had the maximum k of 0.02921 min^{-1}, which was 1.44, 3.04, 2.63, 1.87 and 4.05 times as higher as that of Ag_3PO_4 (0.02024 min^{-1}), (Cs, Rb)$_x$WO$_3$ (0.00962 min^{-1}), g-C_3N_4 (0.01107 min^{-1}), g-C_3N_4 sponges (0.01559 min^{-1}) and CoAl-LDH (0.00722 min^{-1}), respectively.

3.2.2. Photocatalytic degradation of 2-CP and 2-NP

The photocatalytic degradation capability towards 2-CP and 2-NP with Ag_3PO_4, (Cs, Rb)$_x$WO$_3$, g-C_3N_4, g-C_3N_4 sponges, CoAl-LDH and AWCL composite were also investigated. As shown in Fig. 7, in the absence of irradiation (Supporting information Fig. S3.), all the reaction mediums with diverse catalysts presented a negligible amount of degradation towards 2-CP and 2-NP, which presented the sensitivity of catalysts to light and the stability of 2-CP and 2-NP. When exposed to light, the photocatalytic degradation performance dramatically enhanced, the removing capacity for 2-CP of disparate catalysts was put in the following order: the AWCL composite (97.5%) > Ag_3PO_4 (94.1%) > g-C_3N_4 sponges

Table 2
Fitted results of phenol degradation by different photocatalysts

Catalyst	K_{app} (min^{-1})	R^2	Standard error
CoAl-LDH	0.00722	0.95886	0.02069
(Cs, Rb)$_x$WO$_3$	0.00962	0.98562	0.02593
g-C_3N_4	0.01107	0.99645	0.15232
g-C_3N_4 sponges	0.01559	0.98655	0.00362
Ag_3PO_4	0.02024	0.98229	0.00532
AWCL composite	0.02921	0.99439	0.00152

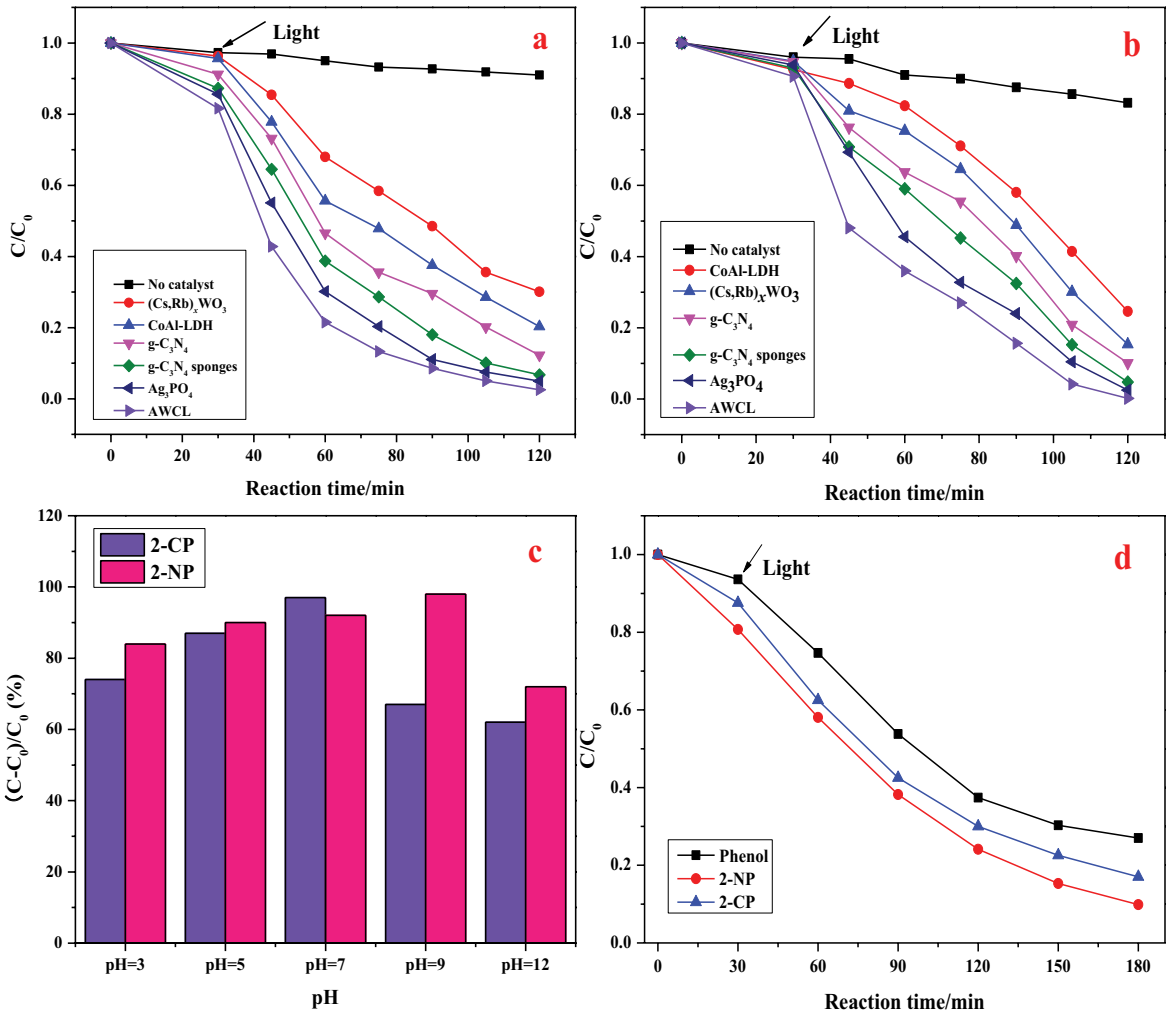

Fig. 7. Photocatalytic degradation of 2-CP (a) and 2-NP (b) with different catalysts, the influence of pH on degradation of 2-CP and 2-NP with AWCL composite (c), and photocatalytic degradation of the mixed solution with AWCL composite (d).

(93.3%) > g-C_3N_4 (87.7%) > CoAl-LDH (79.8%) > (Cs, Rb)$_x$ WO_3 (69.8%) > no catalyst (10.2%), and the degradation towards 2-NP was in a similar order: the AWCL composite (98.5%) > Ag_3PO_4 (97.5%) > g-C_3N_4 sponges (95.1%) > g-C_3N_4 (90.2%) > (Cs, Rb)$_x$$WO_3$ (84.7%) > CoAl-LDH (75.4%) > no catalyst (11.3%).

The influence of disparate pHs on degrading 2-CP and 2-NP was also researched and is presented in Fig. 7c. For 2-CP, there was a similar degradation efficiency trend to phenol, and the order was pH 7 > pH 5 > pH 3 > pH 9 > pH 12. The maximum degradation rate around 97% was reached at a neutral solution, and the tendency was gradually to fall at alkaline pH and to rise at acidic pH. Dissimilarly, as to 2-NP, the excellent photocatalytic efficiency were observed at basic solution (pH = 9) and neutral solution (pH = 7), and the order can be summarized as follows: pH 9 > pH 7 > pH 5 > pH 3 > pH 12.

To assess the kinetics of degrading 2-CP and 2-NP, the first-order model was employed to study the experimental and fitting results (Supporting information Fig. S4). The reaction rate constants (k), coefficient of determinations (R^2), and standard errors obtained through linear fitting and then entered in the supporting information (Tables S1 and S2). In photocatalytic eliminating 2-CP, the k of the AWCL composite (0.03818 L/mg min) was 1.32-, 1.47-, 1.69-, 2.21- and 3.19-fold to that of Ag_3PO_4 (0.02882 L/mg min), g-C_3N_4 sponges (0.02581 L/mg min), g-C_3N_4 (0.02246 L/mg min), CoAl-LDH (0.01731 L/mg min) and (Cs, Rb)$_x$$WO_3$ (0.01196 L/mg min). In photocatalytic exorcising 2-NP, the k of the AWCL composite (0.02595 L/mg min) was 1.31-, 1.57-, 2.21-, 2.61-, and 3.25-fold to that of Ag_3PO_4 (0.01975 L/mg min), g-C_3N_4 sponges (0.01649 L/mg min), g-C_3N_4 (0.01172 L/mg min), (Cs, Rb)$_x$ WO_3 (0.00998 L/mg min) and CoAl-LDH (0.00797 L/mg min). The above results presented an enhanced photocatalytic degradation capacity over the AWCL composite.

3.2.3. Comparative rates of photocatalysis by AWCL composite towards phenol, 2-CP and 2-NP

On the basis of the above experimental results, the most outstanding degradation efficiencies by AWCL composite over phenol, 2-CP and 2-NP were 94.6%, 97.5% and 98.5%

respectively. In the mixed solution, the elapsed time eliminating mixed contaminants was longer relative to degrade individual phenol, 2-CP and 2-NP, and 2-NP was oxidized most thoroughly, according to the situation discussed above (Fig. 7d). The comparative rates of AWCL composite over phenol, 2-CP and 2-NP were concerned with their own structures.

Notoriously, phenols in solutions exist in the form of hydrogen ions and phenoxide anions, and the released hydrogen ions can delocalize the redundant negative charges generated on the aromatic ring to stabilize the structure of phenols. The $–NO_2$ groups in 2-NP and –Cl groups in 2-CP as electron-withdrawing groups can produce (–I) inductive effect to decrease the electron density on the benzene ring, thus reducing the reactivity of phenolic compounds. However, the two substituents are in the ortho position and can be used as electron donors to participate in π-electron conjugation on the benzene ring to increase electron cloud density, therefore reducing the stability of phenolic compounds to oxidants. For phenol, there are no substituents on the aromatic ring to produce an inductive effect and conjugate effect, hence the degradation efficiency over phenol is lower compared with 2-CP and 2-NP.

3.2.4. Photocatalytic mechanism of AWCL composite

For studying the primary reactive species participating in photocatalytic degradation of phenol 2-CP and 2-NP, the effect of multifarious scavengers was explored in irradiation conditions. During the process, ethylenediaminetetraacetic acid (EDTA), isopropyl alcohol (IPA), *p*-benzoquinone (BQ) and dimethyl sulfoxide (DMSO) were used as photogenerated holes (h^+), hydroxyl radical ($^\bullet OH$), superoxide radical ($^\bullet O_2^-$), and electrons (e^-) scavengers, respectively. As shown in Fig. 8, the degradation efficiency of suspensions adding IPA, EDTA, P-BQ, and DMSO were 27.4%, 45.5%, 83.4% and 89.2%, affirm the primary active species was $^\bullet OH$ and $^\bullet O_2^-$ was the secondary active species. The same experiments were carried out with 2-NP and 2-CP, and similar results were obtained (Supporting information Fig. S5).

According to the experiment data and relevant references, the possible degradation mechanism can be proposed as follows [45]. After visible light exposure, the AWCL composite would generate many e^-/h^+ pairs, then the e^- and h^+ would react with H_2O_2, H_2O, OH^- and O_2 to form $^\bullet OH$ and $^\bullet O_2^-$. Simultaneously, the $^\bullet O_2^-$ could be transformed into H_2O_2, $HO_2^\bullet$, sequentially the H_2O_2 would collaborate with e^- to generate $^\bullet OH$. Finally, the phenolic composites will be oxidized into the corresponding degraded products by $^\bullet O_2^-$ and $^\bullet OH$.

$$\text{AWCL} + hv \rightarrow h^+_{vB} + e^-_{CB} \quad (2)$$

$$\text{AWCL}\,(h^+_{vB}) + H_2O \rightarrow {}^\bullet OH + H^+ \quad (3)$$

$$\text{AWCL}\,(h^+_{vB}) + OH^- \rightarrow {}^\bullet OH \quad (4)$$

$$\text{AWCL}\,(e^-_{CB}) + O_2 \rightarrow {}^\bullet O_2^- \quad (5)$$

$$2{}^\bullet O_2^- + 2H^+ \rightarrow H_2O_2 + O_2 \quad (6)$$

$${}^\bullet O_2^- + H^+ \rightarrow HO_2^\bullet \quad (7)$$

$$HO_2^\bullet + 2H^+ \rightarrow H_2O_2 + O_2 \quad (8)$$

$$\text{AWCL}\,(e^-_{CB}) + H_2O_2 \rightarrow {}^\bullet OH + H_2O \quad (9)$$

$${}^\bullet O_2^- + {}^\bullet OH + \text{Phenolic composites} \rightarrow \text{Degraded products} \quad (10)$$

3.2.5. Recyclability study of the AWCL composite

In general, the degradation efficiency of a catalyst will decline after interacting with specific contaminants for several cycles, which determined its recyclability must be tested before practical application. As found in Fig. 9, the AWCL composite still can maintain a degradation rate of over 80% after 5 cycles, indicating the prepared photocatalyst possessed

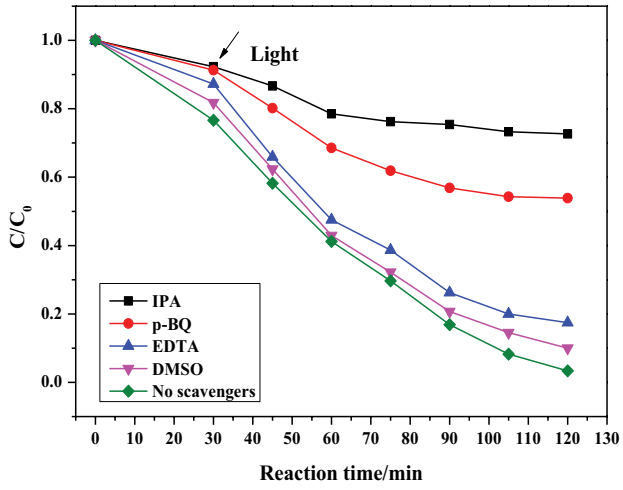

Fig. 8. Scavengers experiment for detecting active species using AWCL composite for phenol degradation.

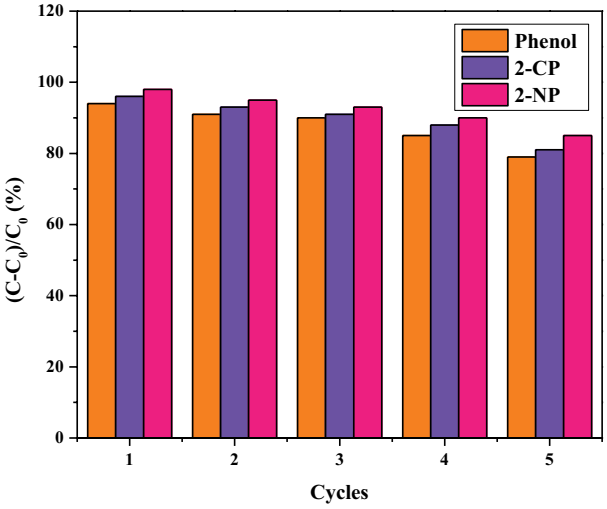

Fig. 9. Reusability study of AWCL composite for phenol, 2-CP and 2-NP degradation.

excellent stability. The lower degradation efficiency was possibly ascribed to that partial photocatalysts were covered by pollutants, reducing the surface active sites and specific surface area and therefore decreasing the activity of catalysts.

4. Conclusion

In summary, the novel porous Ag_3PO_4/(Cs, Rb)$_x$$WO_3$/g-$C_3N_4$/CoAl-LDH composite was prepared successfully. The introduction of Ag_3PO_4 and (Cs, Rb)$_x$$WO_3$ effectively broadened the absorption region of CoAl-LDH, coupling with g-C_3N_4 rendered a high-efficiency physical contact and a strong electronic coupling. These measures endowed Ag_3PO_4/(Cs, Rb)$_x$$WO_3$/g-$C_3N_4$/CoAl-LDH with superior photocatalytic performance over phenol, 2-CP and 2-NP, the degradation efficiency was 94.6%, 97.5% and 98.5% respectively. After five circulation runs, the AWCL composite still can obtain beyond 80% photodegradation rate, indicating the composite possessed favorable reusability and stability. This work opens a new horizon for the preparation of novel photocatalyst for eliminating multiple organic pollutants.

Acknowledgment

The authors are sincerely thankful to the National Natural Science Foundation of China (Nos. 21776319) for providing financial assistance to carry out the research work.

References

[1] Y.H. Chuang, Y.H. Tzou, M.K. Wang, C.H. Liu, P.N. Chiang, Removal of 2-chlorophenol from aqueous solution by Mg/Al layered double hydroxide (LDH) and modified LDH, Ind. Eng. Chem. Res., 47 (2008) 3813–3819.

[2] Y.F. Zhang, S.J. Park, Facile construction of MoO_3@ZIF-8 core-shell nanorods for efficient photoreduction of aqueous Cr(VI), Appl. Catal., B, 240 (2019) 92–101.

[3] C.F. Li, G.Q. Zhao, L.K. Liu, J.G. Yu, X.Y. Jiang, F.P. Jiao, Preparation of CuO_x@ZnFe-LDH composites and photocatalytic degradation of 4-nitrophenol by activated persulfate, J. Mater. Sci. - Mater. Electron., 29 (2018) 19461–19471.

[4] H.K. Bojes, P.G. Pope, Characterization of EPA's 16 priority pollutant polycyclic aromatic hydrocarbons (PAHs) in tank bottom solids and associated contaminated soils at oil exploration and production sites in Texas, Regul. Toxicol. Pharm., 47 (2007) 288–295.

[5] Y.F. Zhang, S.J. Park, Bimetallic AuPd alloy nanoparticles deposited on MoO_3 nanowires for enhanced visible-light driven trichloroethylene degradation, J. Catal., 361 (2018) 238–247.

[6] J.Y. Li, C.C. Chen, J.C. Zhao, H.Y. Zhu, J. Orthman, Photodegradation of dye pollutants on TiO_2 nanoparticles dispersed in silicate under UV-VIS irradiation, Appl. Catal., B, 37 (2002) 331–338.

[7] D. Beyduun, R. Amal, Novel photocatalyst: titania-coated magnetite, activity and photodissolution, J. Phys. Chem. B, 104 (2000) 4387–4396.

[8] H.Y. Li, J. Li, C.C. Xu, P. Yang, D.H.L. Ng, P. Song, M. Zou, Hierarchically porous MoS_2/CoAl-LDH/HCF with synergistic adsorption-photocatalytic performance under visible light irradiation, J. Alloys Compd., 698 (2017) 852–862.

[9] Y. Lu, B. Jiang, L. Fang, F.L. Ling, J.M. Gao, F. Wu, X.H. Zhang, High performance NiFe layered double hydroxide for methyl orange dye and Cr(VI) adsorption, Chemosphere, 152 (2016) 415–422.

[10] S. Kumar, M.A. Isaacs, R. Trofimovaite, L. Durndell, C.M.A. Parlett, R.E. Douthwaite, B. Coulson, M.C.R. Cockett, K. Wilson, A.F. Lee, P25@CoAl layered double hydroxide heterojunction nanocomposites for CO_2 photocatalytic reduction, Appl. Catal., B, 209 (2017) 394–404.

[11] Y.F. Zhang, S.J. Park, Au–Pd bimetallic alloy nanoparticle-decorated $BiPO_4$ nanorods for enhanced photocatalytic oxidation of trichloroethylene, J. Catal., 355 (2017) 1–10.

[12] S.L. Zhao, M. Li, M. Han, D.D. Xu, J. Yang, Y. Lin, N.E. Shi, Y.N. Lu, R. Yang, B.T. Liu, Z.H. Dai, J.C. Bao, Defect-rich Ni_3FeN nanocrystals anchored on N-doped graphene for enhanced electrocatalytic oxygen evolution, Adv. Funct. Mater., 28 (2018) 1706018.

[13] J.F. Ping, Y.X. Wang, Q.P. Lu, B. Chen, J.Z. Chen, Y. Huang, Q.L. Ma, C.L. Tan, J. Yang, X.H. Cao, Z.J. Wang, J. Wu, Y.B. Ying, H. Zhang, Self-assembly of single-layer CoAl-layered double hydroxide nanosheets on 3D graphene network used as highly efficient electrocatalyst for oxygen evolution reaction, Adv. Mater., 28 (2016) 7640–7645.

[14] J.L. Gunjakar, T.W. Kim, H.N. Kim, I.Y. Kim, S.J. Hwang, Mesoporous layer-by-layer ordered nanohybrids of layered double hydroxide and layered metal oxide: highly active visible light photocatalysts with improved chemical stability, J. Am. Chem. Soc., 133 (2011) 14998–15007.

[15] A. Thomas, A. Fischer, F. Goettmann, M. Antonietti, J.O. Muller, R. Schlogl, J.M. Carisson, Graphitic carbon nitride materials: variation of structure and morphology and their use as metal-free catalysts, J. Mater. Chem., 18 (2008) 4893–4908.

[16] S. Nayak, L. Mohapatra, K. Parida, Visible light-driven novel g-C_3N_4/NiFe-LDH composite photocatalyst with enhanced photocatalytic activity towards water oxidation and reduction reaction, J. Mater. Chem. A, 3 (2015) 18622–18635.

[17] S. Nayak, K.M. Parida, Dynamics of charge-transfer behavior in a plasmon-induced quasi-type-II *p-n/n-n* dual heterojunction in Ag@Ag_3PO_4/g-C_3N_4/NiFe LDH nanocomposites for photocatalytic Cr(VI) reduction and phenol oxidation, ACS Omega, 3 (2018) 7324–7343.

[18] J.L. Gunjakar, I.Y. Kim, J.M. Lee, N.S. Lee, S.J. Hwang, Self-assembly of layered double hydroxide 2D nanoplates with graphene nanosheets: an effective way to improve the photocatalytic activity of 2D nanostructured materials for visible light-induced O_2 generation, Energy Environ. Sci., 6 (2013) 1008–1017.

[19] Z.G. Yi, J.H. Ye, N. Kikugawa, T. Kakao, S.X. Ouyang, H.S. Williams, H. Yang, J.Y. Cao, W.J. Luo, Z.S. Li, Y. Liu, R.L. Withers, An orthophosphate semiconductor with photooxidation properties under visible-light irradiation, Nat. Mater., 9 (2010) 559–564.

[20] Z.H. Chen, F. Bing, Q. Liu, Z.G. Zhang, X.M. Fang, Novel Z-scheme visible-light-driven Ag_3PO_4/Ag/SiC photocatalysts with enhanced photocatalytic activity, J. Mater. Chem. A, 3 (2015) 4652–4658.

[21] Y.P. Bi, H.Y. Hu, S.X. Ouyang, G.X. Lu, J.Y. Cao, J.H. Ye, Photocatalytic and photoelectric properties of cubic Ag_3PO_4 sub-microcrystals with sharp corners and edges, Chem. Commun., 48 (2012) 3748–3750.

[22] W. Guo, C.S. Guo, N.N. Zheng, T.D. Sun, S.Q. Liu, Cs_xWO_3 Nanorods coated with polyelectrolyte multilayers as a multifunctional nanomaterial for bimodal imaging-guided photothermal/photodynamic cancer treatment, Adv. Mater., 29 (2017) 1604157.

[23] T.M. Mattox, A. Bergerud, A. Agrawal, D.J. Milliron, Influence of shape on the surface plasmon resonance of tungsten bronze nanocrystals, Chem. Mater., 26 (2014) 1779–1784.

[24] G.L. Li, C.S. Guo, M. Yan, S.Q. Liu, Cs_xWO_3 nanorods: realization of full-spectrum-responsive photocatalytic activities from UV, visible to near-infrared region, Appl. Catal., B, 183 (2016) 142–148.

[25] K. Machida, K. Adachi, Ensemble inhomogeneity of dielectric functions in Cs-doped tungsten oxide nanoparticles, J. Phys. Chem. C, 120 (2016) 16919–16930.

[26] C.X. Yang, J.F. Chen, X.F. Zeng, D.J. Cheng, D.P. Cao, Design of the alkali-metal-doped WO_3 as a near-infrared shielding material for smart window, Ind. Eng. Chem. Res., 53 (2014) 17981–17988.

[27] C.X. Yang, J.F. Chen, X.F. Zeng, D.J. Cheng, H.F. Huang, D.P. Cao, Enhanced near-infrared shielding ability of (Li,K)-codoped WO_3

for smart windows: DFT prediction validated by experiment, Nanotechnology, 27 (2016) 1–7.
[28] Y.C. Jiang, Y. Song, Y.M. Li, W.C. Tian, Z.C. Pan, P.Y. Yang, Y.S. Li, Q.F. Gu, L.F. Hu, Charge transfer in ultrafine LDH nanosheets/graphene interface with superior capacitive energy storage performance, ACS Appl. Mater. Interfaces, 9 (2017) 37645–37654.
[29] Y.D. Li, Z.H. Ruan, Y.Z. He, J.Z. Li, K.Q. Li, Y.Q. Jiang, X.Z. Xu, Y. Yuan, K.F. Lin, *In situ* fabrication of hierarchically porous g-C_3N_4 and understanding on its enhanced photocatalytic activity based on energy absorption, Appl. Catal., B, 236 (2018) 64–75.
[30] J. Guo, C. Dong, L.H. Yang, H. Chen, Crystal structure and superconductivity of rubidium tungsten bronzes Rb_xWO_3 prepared by a hybrid microwave method, Mater. Res. Bull., 43 (2008) 779–786.
[31] G. Tian, X. Zhang, X.P. Zheng, W.Y. Yin, L.F. Ruan, X.D. Liu, L.J. Zhou, L. Yan, S.J. Li, Z.J. Gu, Y.L. Zhao, Multifunctional Rb_xWO_3 nanorods for simultaneous combined chemo-photothermal therapy and photoacoustic/CT imaging, Small, 10 (2014) 4160–4170.
[32] X.Y. Liu, X. Wang, X.T. Yuan, W.J. Dong, F.Q. Huang, Rational composition and structural design of in situ grown nickel-based electrocatalysts for efficient water electrolysis, J. Mater. Chem. A, 4 (2016) 167–172.
[33] Y.B. Dou, S.T. Zhang, T. Pan, S.M. Xu, A.W. Zhou, M. Pu, H. Yan, J.B. Han, M. Wei, D.G. Evans, X. Duan, TiO_2@layered double hydroxide core–shell nanospheres with largely enhanced photocatalytic activity toward O_2 generation, Adv. Funct. Mater., 25 (2015) 2243–2249.
[34] W.H. Bragg, W.L. Bragg, The reflection of X-rays by crystals, Proc. R. Soc. London, Ser. A, 88 (1913) 428–438.
[35] M. Bellardita, E.I. Garcia-Lopez, G. Marci, I. Krivtsov, J.R. Garcia, L. Palmisano, Selective photocatalytic oxidation of aromatic alcohols in water by using P-doped g-C_3N_4, Appl. Catal., B, 220 (2018) 222–233.
[36] X.C. Wang, K. Maeda, A. Thomas, K. Takanabe, G. Xin, J.M. Carlsson, K. Domen, M. Antonietti, A metal-free polymeric photocatalyst for hydrogen production from water under visible light, Nat. Mater., 8 (2009) 76–80.
[37] M.Z. Rahman, J. Zhang, Y.H. Tang, K. Davey, S.Z. Qiao, Graphene oxide coupled carbon nitride homo-heterojunction photocatalyst for enhanced hydrogen production, Mater. Chem. Front., 1 (2017) 562–571.
[38] T. Tyborski, C. Merschjann, S. Orthmann, F. Yang, M.C. Lux-Steiner, T. Schedel-Niedrig, Crystal structure of polymeric carbon nitride and the determination of its process-temperature-induced modifications, J. Phys.: Condens. Matter, 25 (2013) 395402.
[39] F. Fina, S.K. Callear, G.M. Carins, J.T.S. Irvine, Structural investigation of graphitic carbon nitride via XRD and neutron diffraction, Chem. Mater., 27 (2015) 2612–2618.
[40] M.Z. Rahman, P.C. Tapping, T.W. Kee, R. Smernik, N. Spooner, J.L. Moffatt, Y.H. Tang, K. Davey, S.Z. Qiao, A benchmark quantum yield for water photoreduction on amorphous carbon nitride, Adv. Funct. Mater., 27 (2017) 1702384.
[41] Y. Wu, H. Wang, Y.M. Sun, T. Xiao, W.G. Tu, X.Z. Yuan, G.M. Zeng, S.Z. Li, J.W. Chew, Photogenerated charge transfer via interfacial internal electric field for significantly improved photocatalysis in direct Z-scheme oxygen-doped carbon nitrogen/CoAl-layered double hydroxide heterojunction, Appl. Catal., B, 227 (2018) 530–540.
[42] H. Katsumata, T. Sakai, T. Suzuki, S. Kaneco, Highly efficient photocatalytic activity of g-C_3N_4/Ag_3PO_4 hybrid photocatalysts through Z-scheme photocatalytic mechanism under visible light, Ind. Eng. Chem. Res., 53 (2014) 8018–8025.
[43] H. Zhang, G. Wang, D. Chen, X.J. Lv, J.H. Li, Tuning photoelectrochemical performances of Ag-TiO_2 nanocomposites via reduction/oxidation of Ag, Chem. Mater., 20 (2008) 6543–6549.
[44] Y.P. Liu, L. Fang, H.D. Lu, Y.W. Li, C.Z. Hu, H.G. Yu, One-pot pyridineassisted synthesis of visible-light-driven photocatalyst Ag/Ag_3PO_4, Appl. Catal., B, 115 (2012) 245–252.
[45] G.Q. Zhao, X.Q. Chen, J. Zou, C.F. Li, L.K. Liu, T.H. Zhang, J.G. Yu, F.P. Jiao, Activation of peroxymonosulfate by Fe_3O_4–Cs_xWO_3/NiAl layered double hydroxide composites for the degradation of 2,4-dichlorophenoxyacetic acid, Ind. Eng. Chem. Res., 57 (2018) 16308–16317.

Supplementary information

S1. Experimental section

S1.1. Synthesis of CoAl-LDH

In a typical procedure, CoAl-LDH was prepared by a simple hydrothermal method: 0.6 mol $Co(NO_3)_2{\cdot}6H_2O$ and 0.2 mol $Al(NO_3)_3{\cdot}H_2O$ were dissolved into 50 mL deionized water, another solution containing 0.2 mol Na_2CO_3 and 0.1 mol urea were drop-wisely added and subsequently, the mixed solution was translated into a Teflon-lined stainless autoclave to start a hydrothermal reaction at 120°C for 12 h. The final precipitates were obtained through centrifugation, wash and drying at 60°C under static condition overnight.

S1.2. Synthesis of (Cs, Rb)$_x$WO$_3$/CoAl-LDH

In a typical procedure, 0.2 g resultant CoAl-LDH and 0.1 mol WCl_6 were dissolved in 50 mL of anhydrous alcohol with continuous stirring for 20 min at normal temperature. Subsequently, 0.05 mol $CsOH{\cdot}H_2O$, 0.05 mol RbCl and 20 mL acetic acid were added in the sequence listed with stirring and then the mixed solution was put into a Teflon-lined autoclave and afterward by heat-treatment at 200°C for 24 h. After cooling down, the resultant precipitates were collected by centrifuging, washing and drying at 60°C overnight. The pristine $(Cs, Rb)_xWO_3$ was synthesized following a similar method without CoAl-LDH.

S1.3. Synthesis of Ag_3PO_4/(Cs, Rb)$_x$WO$_3$/CoAl-LDH

In the general procedure, 0.2 g $(Cs, Rb)_xWO_3$/CoAl-LDH was dispersed in 100 mL ethanol to ultrasonic dispersion for 1 h. Afterward, a given mass of $AgNO_3$ was added into the dispersion with vigorous stirring for 1 h at dark and subsequently 0.1 mol $(NH4)_2HPO_4$ was dropwise put into for another 2 h. Finally, the whole precipitates were collected by washing, extraction filtration and drying. The pristine Ag_3PO_4 was prepared in the same way without adding $(Cs, Rb)_xWO_3$/CoAl-LDH.

S2. Results and discussion

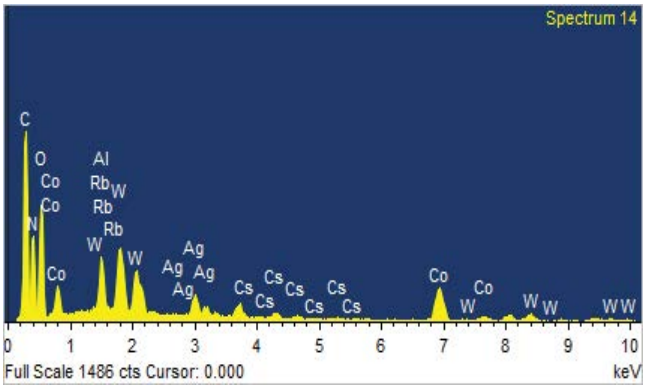

Fig. S1. Energy-dispersive X-ray spectroscopy image of AWCL composite.

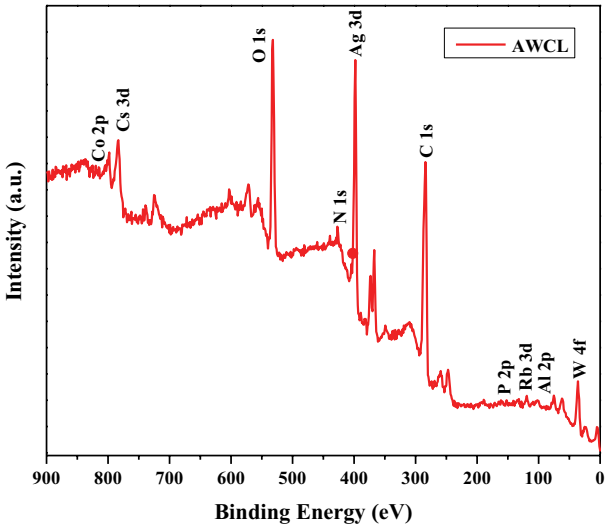

Fig. S2. X-ray photoelectron spectroscopy pattern of AWCL composite.

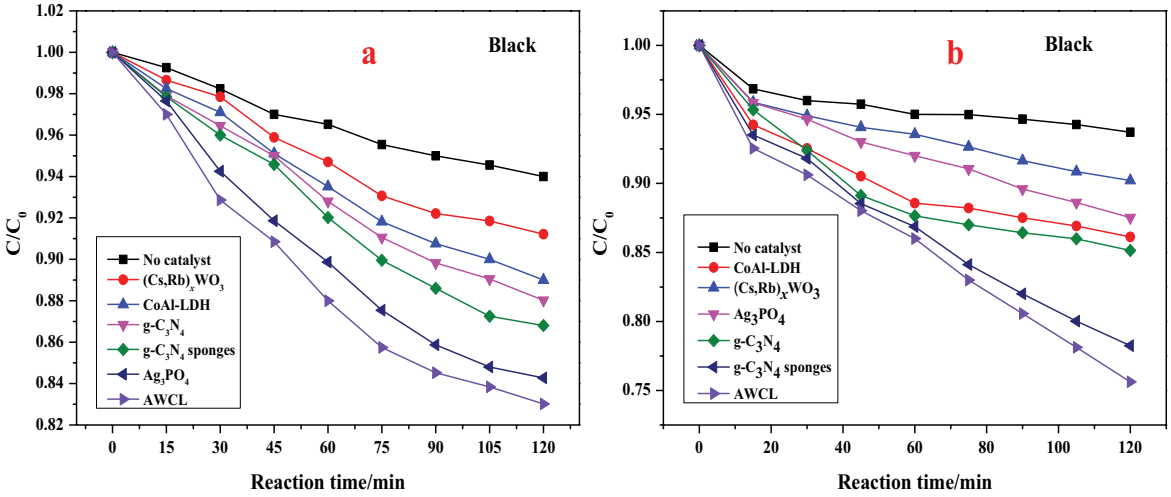

Fig. S3. Photocatalytic degradation of 2-chlorophenol (2-CP) (a) and 2-nitrophenol (2-NP) and (b) with different catalysts in dark.

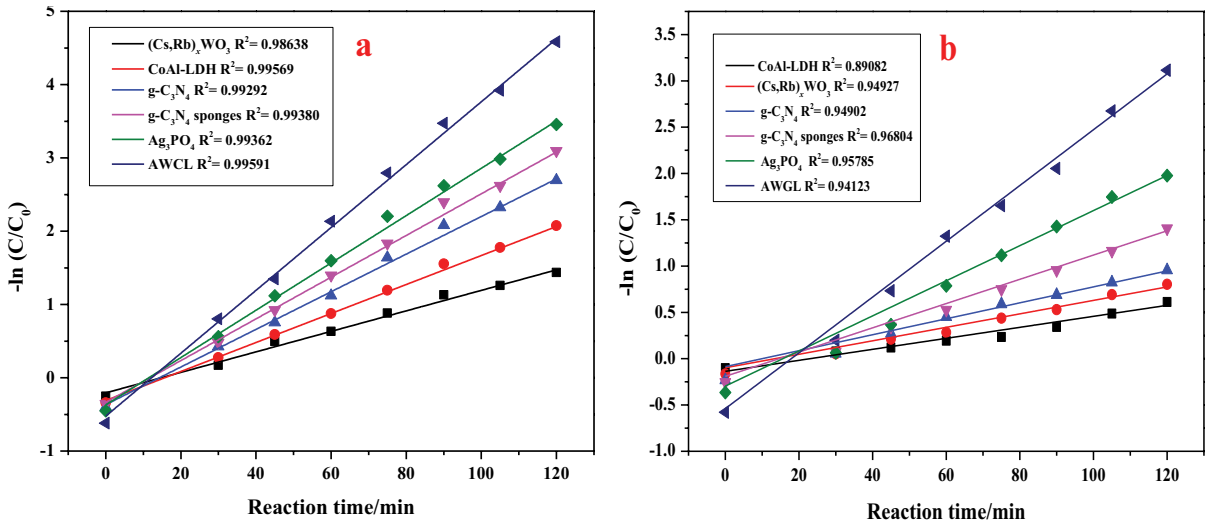

Fig. S4. Pseudo-first-order degradation kinetics for 2-CP (a) and 2-NP (b) with different catalysts.

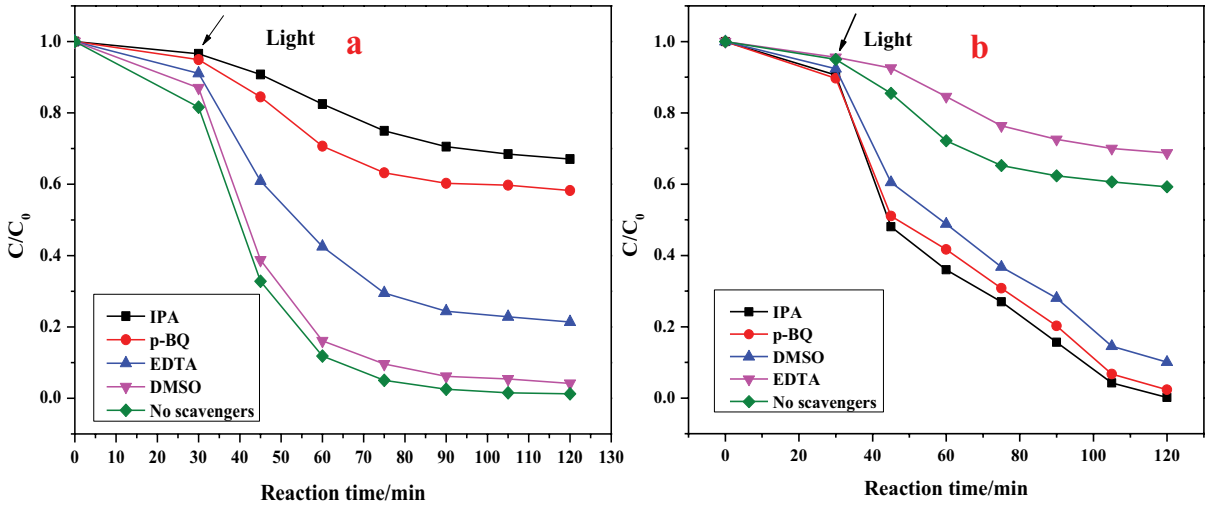

Fig. S5. Scavengers experiment for detecting active species using AWCL composite for 2-CP (a) and 2-NP (b) degradation.

Table S1
Fitted results of 2-CP degradation by different photocatalysts

Catalyst	K_{app} (min^{-1})	R^2	Standard error
(Cs, Rb)$_x$WO$_3$	0.01196	0.98638	0.00324
CoAl-LDH	0.01731	0.99569	0.00398
g-C$_3$N$_4$	0.02246	0.99292	0.00527
g-C$_3$N$_4$ sponges	0.02581	0.99380	0.00585
Ag$_3$PO$_4$	0.02882	0.99362	0.00559
AWCL composite	0.03818	0.99591	0.00721

Table S2
Fitted results of 2-NP degradation by different photocatalysts

Catalyst	K_{app} (min^{-1})	R^2	Standard error
CoAl-LDH	0.00797	0.89082	0.00422
(Cs, Rb)$_x$WO$_3$	0.00998	0.94927	0.00434
g-C$_3$N$_4$	0.01172	0.94902	0.00446
g-C$_3$N$_4$ sponges	0.01649	0.96804	0.00114
Ag$_3$PO$_4$	0.01975	0.95785	0.00165
AWCL composite	0.02595	0.94123	0.00395